

Low-cost INS/GPS with Nonlinear Filtering Methods

Junchuan Zhou

Center for Sensorsystems (ZESS)
University of Siegen
Siegen, Germany.
Zhou@zess.uni-siegen.de

Stefan Knedlik

iMAR GmbH
Im Reihersbruch 3
St. Ingbert, Germany
s.knedlik@imar-navigation.de

Ezzaldeen Edwan

Center for Sensorsystems (ZESS)
University of Siegen
Siegen, Germany.
Edwan@zess.uni-siegen.de

Otmar Loffeld

Center for Sensorsystems (ZESS)
University of Siegen
Siegen, Germany.
Loffeld@zess.uni-siegen.de

Abstract - For land-based navigation, Euler angles are often used in INS/GPS integrated navigation systems. However, the trigonometric operations required in the updates and forming of the rotation matrices for transforming the INS measurements from the body frame to the navigation frame turns the system model to be highly nonlinear. Besides, using low-cost MEMS-based IMUs, the gyroscope bias errors must be correctly estimated and compensated, which makes the nonlinearity problem a critical one. In this contribution, three Kalman filtering methods (i.e., Extended Kalman filter with simplified system model, Extended Kalman filter with linearized system model and Unscented Kalman filter with nonlinear system model) are utilized in INS/GPS tightly-coupled integration. Simulations and field experiments are conducted. Numerical results are compared in terms of both estimation accuracy and processing time.

Keywords: INS/GPS, nonlinear filtering, Euler angles.

1 Introduction

The Global Positioning System (GPS) is widely used in navigation. The GPS receiver can offer long-term stable absolute positioning information with output rate at around 1 to 10 Hz. However, the system performance depends largely on the signal environments. In an inertial navigation system (INS), the angular rate and specific force measurements from the inertial measurement unit (IMU) are processed to yield the position, velocity and attitude solution. Such systems can navigate autonomously and provide measurements at a higher data rate (e.g., 100 Hz). However, the system has to be initialized and calibrated carefully before application. Moreover, the sensor errors are growing unboundedly over time. Due to the complimentary characteristics of GPS and INS, they are often integrated to obtain a complete and continuous navigation solution.

The INS and GPS are often integrated either in loosely-coupled or in tightly-coupled manners. The loosely-

coupled integration has a decentralized estimation architecture, which uses the output of the navigation solutions from a GPS receiver and an INS. The drawbacks are that typically four satellites have to be in view to obtain the updates from the GPS receiver, and the filter cascading problem may occur in case that one Kalman filter (KF) is used for GPS and another is used for integration. In the tightly-coupled integration, only one centralized KF is used, and the pseudorange and delta pseudorange measurements are directly employed in the filter. In such cases, if the number of tracked satellites drops below four, the information from the remaining satellites can still be used to update the INS estimates. Hence, it is considered in this contribution.

Regarding the INS/GPS tightly-coupled integration based on Euler angles, the system dynamic and observation models are both highly nonlinear. The extended Kalman filter (EKF) is considered as the state-of-the-art for fusing the INS and GPS data. However, the filter model relies on the first order linearization of the nonlinear system models. Moreover, the linearization of the nonlinear system models may be a complicated mathematical task. Simplifications are often made when certain rules are met, which will be discussed in Section 3.1. The unscented Kalman filter (UKF) was proposed by Julier as another nonlinear filter. When both the process and measurement noises are Gaussian distributed, its estimation accuracy can reach up to the third order of the Taylor series expansion for any nonlinearity [4]. With the recent advances in computer technology, more advanced nonlinear filtering algorithms can be used in navigation, e.g., the particle filter related algorithms [1]. For accurate attitude determination, extra sensors can be employed. For instance, the integration of an INS with a non-dedicated multi-antenna GPS system using double difference carrier phase measurements are exploited and the results are presented in [3].

In the integration of a single GPS receiver antenna and an INS without redundant attitude information (e.g., from magnetometers, or multi-antenna GPS systems), the INS attitude and sensor bias errors are weakly observable and

are essentially corrected by the GPS velocity measurements through the off-diagonal parameters in the error covariance matrices in the KF. It is the nonlinear system model that relates the attitude errors, sensor bias errors with the position and velocity estimation errors. Therefore, this nonlinearity must be carefully treated when accurate navigation solutions are demanded. However, how severe will this nonlinearity influence the system estimation accuracy? What are the difficulties using an EKF and what is the limitation of the simplified linear system model? Because a thorough analysis on these points has not been found by the authors, in this paper, they will be studied through both simulation tests and field experiments.

In the remainder of this paper, the content is organized as follows. In Section 2, the nonlinear INS process model using Euler angles is given. In Section 3, three approaches for tackling this nonlinearity are introduced. In Section 4, simulations are conducted based on a high dynamic 3D UAV trajectory. In Section 5, a field experiment is made and estimation results are analyzed. Last but not least, a short summary is given at the end of the paper.

2 Nonlinear INS process model with Euler angles

The INS process model we used is often seen for the low-cost micro-electromechanical (MEMS) based IMUs, and it is used as the system dynamic model in INS/GPS integrated navigation systems. For a low-cost IMU, the effects from the earth rotation cannot be observed, and hence, they are not considered in the model. Moreover, in strap-down processing and in the system model for the KF, the transport rate and Coriolis terms have been neglected for simplicity. The simplified mechanization model in discrete time can be expressed in navigation frame as:

$$\mathbf{p}_{n,k+1} = \mathbf{p}_{n,k} + \mathbf{v}_{n,k} \cdot \Delta t \quad (1)$$

$$\mathbf{v}_{n,k+1} = \mathbf{v}_{n,k} + \left[\mathbf{R}_{b2n,k} \cdot (\tilde{\mathbf{f}}_{b,k} - \hat{\mathbf{f}}_{b,k}^{bias}) + \mathbf{g}_n \right] \cdot \Delta t$$

$$\boldsymbol{\psi}_{k+1} = \boldsymbol{\psi}_k + \mathbf{E}_{b2n,k} \cdot (\tilde{\boldsymbol{\omega}}_{b,k} - \hat{\boldsymbol{\omega}}_{b,k}^{bias}) \cdot \Delta t$$

where k is the time instant; $\tilde{\mathbf{f}}_b$ is the measurement vector of the specific force; $\tilde{\boldsymbol{\omega}}_b$ represents the measurement vector of angular rate; \mathbf{g}_n is the local gravity vector; $\boldsymbol{\psi}$ is the Euler angles; \mathbf{R}_{b2n} is the frame rotation matrix from body frame to north east and down (NED) navigation frame, and \mathbf{E}_{b2n} is the rotation rate transformation matrix between body and navigation frame.

$$\mathbf{R}_{b2n} = \begin{pmatrix} C\varphi C\phi & C\varphi S\phi S\theta - S\varphi C\theta & C\varphi S\phi C\theta + S\varphi S\theta \\ S\varphi C\phi & S\varphi S\phi S\theta + C\varphi C\theta & S\varphi S\phi C\theta - C\varphi S\theta \\ -S\phi & C\phi S\theta & C\phi C\theta \end{pmatrix} \quad (2)$$

$$\mathbf{E}_{b2n} = \begin{pmatrix} 1 & S\theta T\phi & C\theta T\phi \\ 0 & C\theta & -S\theta \\ 0 & S\theta / C\phi & C\theta / C\phi \end{pmatrix}$$

where CX , SX and TX represent the trigonometric operations of cosine, sine and tangent respectively. The θ, ϕ, φ denote the roll, pitch and yaw. The $\hat{\mathbf{f}}_{b,k}^{bias}$ and $\hat{\boldsymbol{\omega}}_{b,k}^{bias}$ in Equation (1) are the estimated specific force and angular rate bias errors. These bias errors have non-Gaussian characteristics and must be estimated and corrected carefully. For low-cost MEMS-based IMUs, the gyro bias errors are critical. This is due to the fact that they will be integrated to form the Euler angles, which are then used to build the vector transformation matrices for transforming the accelerometer measurements from the body frame to the navigation frame. After integrations, these errors turn out to be the position and velocity drifts in the navigation frame [9].

3 Kalman filtering methods

Three Kalman filtering methods are compared in this paper, which are the EKF with simplified system model; the EKF with linearized system model and the UKF with nonlinear system model.

3.1 EKF with simplified system model

The direct linearization of Equation (1) is difficult due to the trigonometric operations contained in \mathbf{R}_{b2n} and \mathbf{E}_{b2n} . Simplifications can be made when the following rules are met:

- 1) Accurate INS self alignment and calibration processes are conducted before the application.
- 2) The angular changes between INS data update interval are small so that small angle assumptions, i.e., $\cos(\delta\theta) \approx 1$ and $\sin(\delta\theta) \approx \delta\theta$, can be made.

Fulfilling the above requirements, the simplified discrete-time linear system model is given in Equation (3). The error states are used, which include the position and velocity estimation errors in NED navigation frame; attitude errors (i.e., roll, pitch and yaw); accelerometers and gyro bias errors in body frame and receiver clock bias and clock drift errors in distance.

$$\begin{bmatrix} \delta\mathbf{p}_{k+1} \\ \delta\mathbf{v}_{k+1} \\ \delta\boldsymbol{\psi}_{k+1} \\ \delta\mathbf{f}_{k+1} \\ \delta\boldsymbol{\omega}_{k+1} \\ c\delta\tilde{t}_{k+1} \\ c\delta\tilde{t}'_{k+1} \end{bmatrix} = \begin{bmatrix} \mathbf{I}_{3\times3} & \mathbf{I}_{3\times3}\Delta t & \mathbf{O}_{3\times3} & \mathbf{O}_{3\times3} & \mathbf{O}_{3\times3} & \mathbf{0}_{3\times1} & \mathbf{0}_{3\times1} \\ \mathbf{O}_{3\times3} & \mathbf{I}_{3\times3} & [\hat{\mathbf{f}}_n \times] \Delta t & \mathbf{R}_{b2n} \Delta t & \mathbf{O}_{3\times3} & \mathbf{0}_{3\times1} & \mathbf{0}_{3\times1} \\ \mathbf{O}_{3\times3} & \mathbf{O}_{3\times3} & \mathbf{I}_{3\times3} & \mathbf{O}_{3\times3} & -\mathbf{R}_{b2n} \Delta t & \mathbf{0}_{3\times1} & \mathbf{0}_{3\times1} \\ \mathbf{O}_{3\times3} & \mathbf{O}_{3\times3} & \mathbf{O}_{3\times3} & \mathbf{I}_{3\times3} & \mathbf{O}_{3\times3} & \mathbf{0}_{3\times1} & \mathbf{0}_{3\times1} \\ \mathbf{O}_{3\times3} & \mathbf{O}_{3\times3} & \mathbf{O}_{3\times3} & \mathbf{O}_{3\times3} & \mathbf{I}_{3\times3} & \mathbf{0}_{3\times1} & \mathbf{0}_{3\times1} \\ \mathbf{0}_{3\times1}^T & \mathbf{0}_{3\times1}^T & \mathbf{0}_{3\times1}^T & \mathbf{0}_{3\times1}^T & \mathbf{0}_{3\times1}^T & 1 & \Delta t \\ \mathbf{0}_{3\times1}^T & \mathbf{0}_{3\times1}^T & \mathbf{0}_{3\times1}^T & \mathbf{0}_{3\times1}^T & \mathbf{0}_{3\times1}^T & 0 & 1 \end{bmatrix} \cdot \begin{bmatrix} \delta\mathbf{p}_k \\ \delta\mathbf{v}_k \\ \delta\boldsymbol{\psi}_k \\ \delta\mathbf{f}_k \\ \delta\boldsymbol{\omega}_k \\ c\delta\tilde{t}_k \\ c\delta\tilde{t}'_k \end{bmatrix} + \mathbf{w}_k \quad (3)$$

where $[\hat{\mathbf{f}}_n \times]$ is the skew-symmetric matrix of $\hat{\mathbf{f}}_n = \mathbf{R}_{b2n} \hat{\mathbf{f}}_b$, and $\hat{\mathbf{f}}_b = \tilde{\mathbf{f}}_b - \hat{\mathbf{f}}_b^{bias}$. The unknown time-varying gyroscope and accelerometer bias errors $\delta\mathbf{f}_b$ and $\delta\boldsymbol{\omega}_b$ are modeled as random-walk plus constant [5]. The receiver clock drift error $c\delta\tilde{t}$ is modeled as random walk, while the receiver clock bias $c\delta\tilde{t}'$ is the integral of the clock drift error. The derivations of Equation (3) are encountered often in literature, and the equations shown in this section follow [6-7].

In the inertial frame, the inertial acceleration $\dot{\mathbf{v}}_i$ measured on the Earth is equal to the acceleration measured by the accelerometers $\tilde{\mathbf{f}}_i$ compensated for the Earth's gravity \mathbf{g}_i , Coriolis acceleration $\boldsymbol{\omega}_{ie}^i \times \mathbf{v}_i$ and centripetal acceleration $\boldsymbol{\omega}_{ie}^i \times \boldsymbol{\omega}_{ie}^i \times \mathbf{r}$ as:

$$\dot{\mathbf{v}}_i = \tilde{\mathbf{f}}_i + \mathbf{g}_i - (\boldsymbol{\omega}_{ie}^i \times \boldsymbol{\omega}_{ie}^i \times \mathbf{r}) - (\boldsymbol{\omega}_{ie}^i \times \mathbf{v}_i) \quad (4)$$

where $\boldsymbol{\omega}_{ie}^i$ is the earth rotation with respect to the inertial frame, and \mathbf{v}_i is the earth-relative velocity expressed in the inertial frame.

In the earth frame, the acceleration of the vehicle $\dot{\mathbf{v}}_e$ with respect to the earth is equal to the inertial acceleration of the vehicle $\dot{\mathbf{v}}_i$ transformed over to the earth frame minus the Coriolis acceleration $\boldsymbol{\omega}_{ie}^i \times \mathbf{v}_e$ due to the velocity \mathbf{v}_e of the vehicle over a rotating earth:

$$\dot{\mathbf{v}}_e = \mathbf{R}_{ie} \dot{\mathbf{v}}_i - \boldsymbol{\omega}_{ie}^i \times \mathbf{v}_e \quad (5)$$

For the low-cost MEMS-based IMU, the earth rotation cannot be detected. Thus, substituting Equation (4) in Equation (5) with $\boldsymbol{\omega}_{ie}^i$ equals to zero vector:

$$\dot{\mathbf{v}}_e = \tilde{\mathbf{f}}_e + \mathbf{g}_e \quad (6)$$

where $\tilde{\mathbf{f}}_e$ represents the acceleration measured by the accelerometers in the body frame expressed in the earth frame. With constant gravity vector, by the definition of perturbation, we arrive at:

$$\delta \dot{\mathbf{v}}_e = \hat{\mathbf{v}}_e - \dot{\mathbf{v}}_e = \hat{\mathbf{R}}_{b2e} \hat{\mathbf{f}}_b - \mathbf{R}_{b2e} \tilde{\mathbf{f}}_b \quad (7)$$

The direction cosine matrix $\hat{\mathbf{R}}_{b2e}$ is the true transformation matrix \mathbf{R}_{b2e} misaligned by the small misalignment angles $[\delta\boldsymbol{\psi} \times]$ as:

$$\hat{\mathbf{R}}_{b2e} = (\mathbf{I}_{3 \times 3} - [\delta\boldsymbol{\psi} \times]) \mathbf{R}_{b2e} \quad (8)$$

Substituting Equation (8) into Equation (7) yields:

$$\begin{aligned} \delta \dot{\mathbf{v}}_e &= (\mathbf{R}_{b2e} - [\delta\boldsymbol{\psi} \times] \mathbf{R}_{b2e}) \hat{\mathbf{f}}_b - \mathbf{R}_{b2e} \tilde{\mathbf{f}}_b \\ &= \mathbf{R}_{b2e} \delta \hat{\mathbf{f}}_b - [\delta\boldsymbol{\psi} \times] \hat{\mathbf{f}}_e = \mathbf{R}_{b2e} \delta \hat{\mathbf{f}}_b + [\hat{\mathbf{f}}_e \times] \delta \boldsymbol{\psi} \end{aligned} \quad (9)$$

where $\delta \hat{\mathbf{f}}_b = \hat{\mathbf{f}}_b - \tilde{\mathbf{f}}_b$, and $[\delta\boldsymbol{\psi} \times] \hat{\mathbf{f}}_e = -[\hat{\mathbf{f}}_e \times] \delta \boldsymbol{\psi}$.

Rearranging Equation (8) yields:

$$[\delta\boldsymbol{\psi} \times] = \mathbf{I}_{3 \times 3} - \hat{\mathbf{R}}_{b2e} \mathbf{R}_{b2e}^T \quad (10)$$

After differentiating we have:

$$[\delta\dot{\boldsymbol{\psi}} \times] = -\hat{\mathbf{R}}_{b2e} \dot{\mathbf{R}}_{b2e}^T - \hat{\mathbf{R}}_{b2e} \mathbf{R}_{b2e}^T \quad (11)$$

With small angle transformations, the derivative of the direction-cosine matrix can be formulated as:

$$\dot{\mathbf{R}}_{b2e} = \mathbf{R}_{b2e} \boldsymbol{\Omega}_{be}^b \text{ and } \hat{\mathbf{R}}_{b2e} = \hat{\mathbf{R}}_{b2e} \hat{\boldsymbol{\Omega}}_{be}^b \quad (12)$$

where $\boldsymbol{\Omega}_{be}^b$ and $\hat{\boldsymbol{\Omega}}_{be}^b$ are the skew-symmetric representation of the angular rotation rate vector in the body frame with respect to the earth frame.

Substituting Equation (12) into Equation (11) gives:

$$\begin{aligned} [\delta\dot{\boldsymbol{\psi}} \times] &= -\hat{\mathbf{R}}_{b2e} ([\boldsymbol{\Omega}_{be}^b]^T + \hat{\boldsymbol{\Omega}}_{be}^b) \mathbf{R}_{b2e}^T \\ &= -\hat{\mathbf{R}}_{b2e} \delta \boldsymbol{\Omega}_{be}^b \mathbf{R}_{b2e}^T \end{aligned} \quad (13)$$

For the skew symmetric matrix $\boldsymbol{\Omega}_{be}^b$, we have $[\boldsymbol{\Omega}_{be}^b]^T = -\boldsymbol{\Omega}_{be}^b$, and let $\delta \boldsymbol{\Omega}_{be}^b = \hat{\boldsymbol{\Omega}}_{be}^b - \boldsymbol{\Omega}_{be}^b$. Substituting Equation (8) in Equation (13) yields:

$$\begin{aligned} [\delta\dot{\boldsymbol{\psi}} \times] &= -(\mathbf{I}_{3 \times 3} - [\delta\boldsymbol{\psi} \times]) \mathbf{R}_{b2e} \delta \boldsymbol{\Omega}_{be}^b \mathbf{R}_{b2e}^T \\ &= -\mathbf{R}_{b2e} \delta \boldsymbol{\Omega}_{be}^b \mathbf{R}_{b2e}^T + [\delta\boldsymbol{\psi} \times] \mathbf{R}_{b2e} \delta \boldsymbol{\Omega}_{be}^b \mathbf{R}_{b2e}^T \end{aligned} \quad (14)$$

The product of $[\delta\boldsymbol{\psi} \times] \mathbf{R}_{b2e} \delta \boldsymbol{\Omega}_{be}^b \mathbf{R}_{b2e}^T$ is negligible due to the small terms $[\delta\boldsymbol{\psi} \times]$ and $\delta \boldsymbol{\Omega}_{be}^b$. Thus, we have:

$$[\delta\dot{\boldsymbol{\psi}} \times] = -\mathbf{R}_{b2e} \delta \boldsymbol{\Omega}_{be}^b \mathbf{R}_{b2e}^T = -[\mathbf{R}_{b2e} \delta \boldsymbol{\omega}_{be}^b \times] \quad (15)$$

While the gyroscope measures the total inertial rotation $\boldsymbol{\omega}_{ib}^b$ which comprises $\boldsymbol{\omega}_{be}^b$ plus rotation of the earth with respect to the inertial frame expressed in the body frame. Thus the following relationship exists:

$$\boldsymbol{\omega}_{be}^b = \boldsymbol{\omega}_{ib}^b - \mathbf{R}_{i2b} \boldsymbol{\omega}_{ie}^i \quad (16)$$

The earth rotation rate is considered as constant, i.e., $\boldsymbol{\omega}_{ie}^i = \mathbf{0}$. Thus, we have $\delta \boldsymbol{\omega}_{be}^b \approx \delta \boldsymbol{\omega}_{ib}^b$. Substituting this in Equation (15), we get:

$$[\delta\dot{\boldsymbol{\psi}} \times] = -[\mathbf{R}_{b2e} \delta \boldsymbol{\omega}_{ib}^b \times] \Rightarrow \delta \dot{\boldsymbol{\psi}} = -\mathbf{R}_{b2e} \delta \boldsymbol{\omega}_{ib}^b \quad (17)$$

Having the Equations (9) and (17), and denoting the $\delta \boldsymbol{\omega}_{ib}^b$ as $\delta \boldsymbol{\omega}_b$ for simplicity, the inertial error models can be formed as:

$$\delta \dot{\mathbf{p}} = \delta \mathbf{v} \quad (18)$$

$$\delta \dot{\mathbf{v}} = [\hat{\mathbf{f}}_e \times] \delta \boldsymbol{\psi} + \mathbf{R}_{b2e} \delta \hat{\mathbf{f}}_b$$

$$\delta \dot{\boldsymbol{\psi}} = -\mathbf{R}_{b2e} \delta \boldsymbol{\omega}_b$$

The NED navigation frame is a type of earth frame and often used for land vehicle applications. Hence, it is used in this contribution. Equation (18) is in the continuous time domain. The discrete-time system transition matrix is given in Equation (3).

3.2 EKF with linearized system model

In this method, the error states are still used, which are given in Section 3.1. The nonlinear INS process model is shown in Equation (1). The linearization is conducted at the updated trajectory during the run-time. The derivation of the Jacobian matrix for this nonlinear system model (i.e., with respect to the current updated position, velocity, attitude, accelerometer bias, gyro bias, clock bias and clock drift estimates) is a complicated mathematical task, which is shown in Equation (19).

$$\mathbf{F}_{Jacobian} = \begin{bmatrix} \mathbf{I}_{3 \times 3} & \mathbf{I}_{3 \times 3} \Delta t & \mathbf{O}_{3 \times 3} & \mathbf{O}_{3 \times 3} & \mathbf{O}_{3 \times 3} & \mathbf{0}_{3 \times 1} & \mathbf{0}_{3 \times 1} \\ \mathbf{O}_{3 \times 3} & \mathbf{I}_{3 \times 3} & \mathbf{F}_{23} & \mathbf{F}_{24} & \mathbf{O}_{3 \times 3} & \mathbf{0}_{3 \times 1} & \mathbf{0}_{3 \times 1} \\ \mathbf{O}_{3 \times 3} & \mathbf{O}_{3 \times 3} & \mathbf{F}_{33} & \mathbf{O}_{3 \times 3} & -\mathbf{F}_{35} & \mathbf{0}_{3 \times 1} & \mathbf{0}_{3 \times 1} \\ \mathbf{O}_{3 \times 3} & \mathbf{O}_{3 \times 3} & \mathbf{O}_{3 \times 3} & \mathbf{I}_{3 \times 3} & \mathbf{O}_{3 \times 3} & \mathbf{0}_{3 \times 1} & \mathbf{0}_{3 \times 1} \\ \mathbf{O}_{3 \times 3} & \mathbf{O}_{3 \times 3} & \mathbf{O}_{3 \times 3} & \mathbf{O}_{3 \times 3} & \mathbf{I}_{3 \times 3} & \mathbf{0}_{3 \times 1} & \mathbf{0}_{3 \times 1} \\ \mathbf{0}_{3 \times 1}^T & \mathbf{0}_{3 \times 1}^T & \mathbf{0}_{3 \times 1}^T & \mathbf{0}_{3 \times 1}^T & \mathbf{0}_{3 \times 1}^T & 1 & \Delta t \\ \mathbf{0}_{3 \times 1}^T & \mathbf{0}_{3 \times 1}^T & \mathbf{0}_{3 \times 1}^T & \mathbf{0}_{3 \times 1}^T & \mathbf{0}_{3 \times 1}^T & 0 & 1 \end{bmatrix} \quad (19)$$

where

$$\mathbf{F}_{23} = \begin{bmatrix} \hat{f}_y(S\theta S\phi + C\theta C\phi S\phi) & \hat{f}_z C\phi C\theta C\phi & \hat{f}_z(C\phi S\theta + C\theta S\phi S\phi) \\ +\hat{f}_z(C\theta S\phi + C\phi S\phi S\theta) & -\hat{f}_z C\phi S\phi & -\hat{f}_y(C\theta C\phi - S\phi S\theta S\phi) \\ -\hat{f}_z(S\phi S\theta S\phi + C\theta C\phi) & \hat{f}_z C\phi C\theta S\phi & \hat{f}_z(S\theta S\phi + C\theta C\phi S\phi) \\ -\hat{f}_y(C\phi S\theta - C\theta S\phi S\phi) & -\hat{f}_z S\phi S\phi & -\hat{f}_y(C\theta S\phi - C\phi S\phi S\theta) \\ \hat{f}_y C\phi C\theta - \hat{f}_z C\phi S\theta & -\hat{f}_z C\phi & 0 \\ & -\hat{f}_z C\theta S\phi & \\ & -\hat{f}_y S\phi S\theta & \end{bmatrix} \Delta t \quad (20)$$

$$\mathbf{F}_{24} = \begin{bmatrix} -C\phi C\phi & C\theta S\phi - C\phi S\phi S\theta & -S\theta S\phi - C\theta C\phi S\phi \\ -C\phi S\phi & -C\theta C\phi - S\phi S\theta S\phi & C\phi S\theta - C\theta S\phi S\phi \\ S\phi & -C\phi S\theta & -C\phi C\theta \end{bmatrix} \Delta t \quad (21)$$

and

$$\mathbf{F}_{33} = \begin{bmatrix} 1 + \begin{bmatrix} \hat{\omega}_y C\theta T\phi \\ +\hat{\omega}_z T\phi S\theta \end{bmatrix} \Delta t & \begin{bmatrix} \hat{\omega}_z C\theta(T^2\phi + 1) \\ +\hat{\omega}_y S\theta(T^2\phi + 1) \end{bmatrix} \Delta t & 0 \\ -\begin{bmatrix} \hat{\omega}_z C\theta \\ +\hat{\omega}_y S\theta \end{bmatrix} \Delta t & 1 & 0 \\ \begin{bmatrix} \hat{\omega}_y C\theta - \hat{\omega}_z S\theta \\ C\phi \end{bmatrix} \Delta t & \begin{bmatrix} C\theta S\phi \hat{\omega}_z + S\phi S\theta \hat{\omega}_y \\ C^2\phi \end{bmatrix} \Delta t & 1 \end{bmatrix} \quad (22)$$

and

$$\mathbf{F}_{35} = \begin{bmatrix} 1 & T\phi S\theta & C\theta T\phi \\ 0 & C\theta & -S\theta \\ 0 & S\theta/C\phi & C\theta/C\phi \end{bmatrix} \Delta t \quad (23)$$

where $\hat{f}_x = \tilde{f}_x - \hat{f}_x^{bias}$, $\hat{f}_y = \tilde{f}_y - \hat{f}_y^{bias}$, $\hat{f}_z = \tilde{f}_z - \hat{f}_z^{bias}$, $\hat{\omega}_y = \tilde{\omega}_y - \hat{\omega}_y^{bias}$, $\hat{\omega}_z = \tilde{\omega}_z - \hat{\omega}_z^{bias}$ are the IMU raw data compensated with the estimated sensor bias errors expressed in the body frame; CX, SX and TX are the mathematical operations of cosine, sine and tangent respectively, and C^2X, T^2X represent the square of cosine and tangent operations. The linearization is accomplished using the ‘‘Jacobian’’ function in MATLAB.

3.3 UKF with nonlinear system model

In the UKF algorithm, the nonlinear system models are directly applied to the sigma points to yield their transformed state vectors, from which the *a priori* and *a posteriori* estimates are derived. Total states are used in this method. Consider the case that the system process and measurement noises are additive and Gaussian distributed:

$$\mathbf{x}_k = \mathbf{f}_{k-1}(\mathbf{x}_{k-1}) + \mathbf{w}_{k-1} \quad (24)$$

$$\mathbf{y}_k = \mathbf{h}_k(\mathbf{x}_k) + \mathbf{v}_k$$

with $\mathbf{w}_k \sim \mathcal{N}(0, \mathbf{Q}_k)$, and $\mathbf{v}_k \sim \mathcal{N}(0, \mathbf{R}_k)$

The following algorithm from [4,10] is used in this paper:

1) Initialization

$$\hat{\mathbf{x}}_0^+ = E(\mathbf{x}_0), \mathbf{P}_0^+ = E[(\mathbf{x}_0 - \hat{\mathbf{x}}_0^+)(\mathbf{x}_0 - \hat{\mathbf{x}}_0^+)^T] \quad (25)$$

2) Draw sigma points

$$\boldsymbol{\chi}_i = \hat{\mathbf{x}}_{k-1}^+ + \left(\sqrt{n\mathbf{P}_{k-1}^+}\right)_i^T, \boldsymbol{\chi}_{i+n} = \hat{\mathbf{x}}_{k-1}^+ - \left(\sqrt{n\mathbf{P}_{k-1}^+}\right)_i^T, i=1, \dots, n \quad (26)$$

3) Time update

$$\hat{\mathbf{x}}_k^- = \frac{1}{2n} \sum_{i=1}^{2n} \mathbf{f}_{k-1}(\boldsymbol{\chi}_i), \quad (27)$$

$$\mathbf{P}_k^- = \frac{1}{2n} \sum_{i=1}^{2n} [\mathbf{f}_{k-1}(\boldsymbol{\chi}_i) - \hat{\mathbf{x}}_k^-][\mathbf{f}_{k-1}(\boldsymbol{\chi}_i) - \hat{\mathbf{x}}_k^-]^T + \mathbf{Q}_{k-1}$$

4) Draw sigma points

$$\boldsymbol{\chi}_i = \hat{\mathbf{x}}_k^- + \left(\sqrt{n\mathbf{P}_k^-}\right)_i^T, \boldsymbol{\chi}_{i+n} = \hat{\mathbf{x}}_k^- - \left(\sqrt{n\mathbf{P}_k^-}\right)_i^T, i=1, \dots, n \quad (28)$$

5) Predict measurements

$$\hat{\mathbf{y}}_k = \frac{1}{2n} \sum_{i=1}^{2n} \mathbf{h}_k(\boldsymbol{\chi}_i) \quad (29)$$

6) Update covariance

$$\mathbf{P}_k^{xy} = \frac{1}{2n} \sum_{i=1}^{2n} [\mathbf{h}_k(\boldsymbol{\chi}_i) - \hat{\mathbf{y}}_k][\mathbf{h}_k(\boldsymbol{\chi}_i) - \hat{\mathbf{y}}_k]^T + \mathbf{R}_k \quad (30)$$

$$\mathbf{P}_k^{yy} = \frac{1}{2n} \sum_{i=1}^{2n} [\boldsymbol{\chi}_i - \hat{\mathbf{x}}_k^-][\mathbf{h}_k(\boldsymbol{\chi}_i) - \hat{\mathbf{y}}_k]^T$$

7) Measurement update

$$\mathbf{K}_k = \mathbf{P}_k^{xy} (\mathbf{P}_k^{yy})^{-1} \quad (31)$$

$$\hat{\mathbf{x}}_k^+ = \hat{\mathbf{x}}_k^- + \mathbf{K}_k (\tilde{\mathbf{y}}_k - \hat{\mathbf{y}}_k)$$

$$\mathbf{P}_k^+ = \mathbf{P}_k^- - \mathbf{K}_k \mathbf{P}_k^{yy} \mathbf{K}_k^T$$

where ‘n’ denotes the dimension of the system state vector. $\left(\sqrt{n\mathbf{P}_{k-1}^+}\right)$ is the matrix square root of $n\mathbf{P}_{k-1}^+$, such as $\left(\sqrt{n\mathbf{P}_{k-1}^+}\right)^T \left(\sqrt{n\mathbf{P}_{k-1}^+}\right) = n\mathbf{P}_{k-1}^+$, which can be obtained from the Cholesky factorization ‘CHOL’ in MATLAB. $\left(\sqrt{n\mathbf{P}_{k-1}^+}\right)_i$ is the *i*-th row of $\left(\sqrt{n\mathbf{P}_{k-1}^+}\right)$. $\left(\sqrt{n\mathbf{P}_{k-1}^+}\right)_i^T$ is the transpose of $\left(\sqrt{n\mathbf{P}_{k-1}^+}\right)_i$. \mathbf{Q}_k is the covariance matrix of the additive system process noise. \mathbf{R}_k is the covariance matrix of the additive measurement noise.

4 Simulation Test

In this test, a 3D UAV trajectory is used as shown in Figure 1. The velocity dynamic profile is plotted in Figure 2. The UAV is flying at the norm velocity of 40 m/s, which is 144 km/h. In the north and east directions, the velocities vary dramatically from approximately +40 m/s to -40 m/s just in a few seconds.

This trajectory is derived from the strapdown processing of the field collected high quality IMU raw data. It is considered as the reference for generating GPS measurements (i.e., pseudorange and Doppler, where the Doppler measurement is derived from the first order central difference of the carrier-phase data $d_k^{(n)} \approx (\phi_{k+1}^{(n)} - \phi_{k-1}^{(n)}) / (2 \cdot \Delta t)$) using the SATNAV toolbox from GPSofSoft LLC. It needs to be noted that such an approximation of instantaneous Doppler measurements using carrier phase data at low output rate (i.e., 1 Hz or 5 Hz) is very poor for high dynamic applications [8]. One

solution proposed by the author on this problem is presented in [2]. In this paper, we simply use 50 Hz carrier phase data to derive the Doppler measurements.

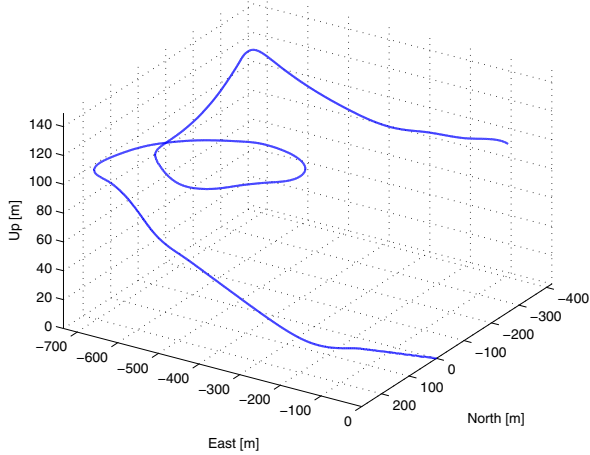


Figure 1. UAV trajectory.

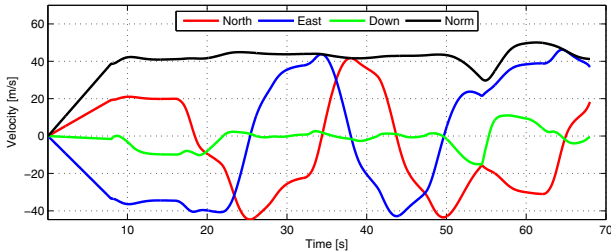


Figure 2. Velocity dynamic profile.

For the INS/GPS integration, we assume that a NovAtel DL-4plus GPS receiver is used. From the specification, we know that when the receiver is navigating under benign signal environment, in differential GPS mode, the typical values for position and velocity estimation errors are 0.45 m CEP and 0.03 m/s RMS respectively. Hence, we reasonably simulate 0.5 m (1σ) thermal noise errors on the pseudorange, and 0.02 m/s (1σ) thermal noise errors on the Doppler measurements. For the multipath, we use the SATNAV toolbox to generate the errors. The parameters we have chosen are 0.4 m (1σ) for generating multipath errors on pseudorange, and 0.01 m/s (1σ) for generating errors on the Doppler. Time constant is chosen to be 15 s. Regarding the IMU, an automotive level MEMS-IMU is simulated. The main sensor errors are shown in Table 1.

Table 1. Error statistics of the simulated IMU data (1σ).

Gyroscope (Angular rates)	Bias stability	Noise (ARW)
	3600 [$^{\circ}$ /h]	0.05 [$^{\circ}$ /s/ $\sqrt{\text{Hz}}$]
Accelerometer (Specific forces)	Bias stability	Noise (VRW)
	2400 [μg]	1000 [μg / $\sqrt{\text{Hz}}$]

The IMU raw data (simulated errors plus the field collected high quality IMU raw data) in body frame are plotted in Figure 3.

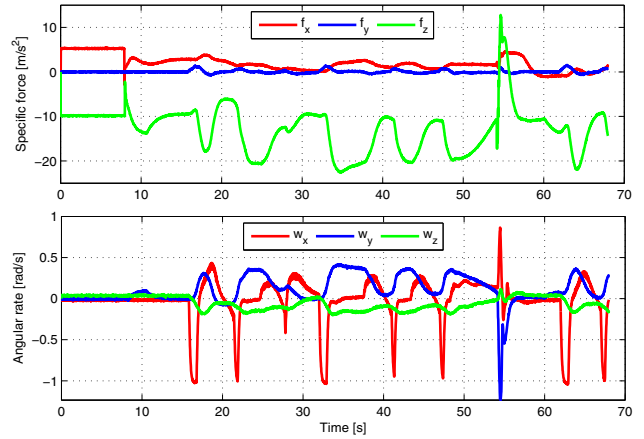


Figure 3. IMU raw data.

For the integrated KF, the system time-update happens at the IMU data update rate, which is 50 Hz, while the system measurement update happens at the GPS data update rate, which is 5 Hz. The simulation is conducted with 8 satellites in view. The 100 s INS self alignment and calibration process is conducted before the simulation. The attitude estimation errors are plotted in Figure 4. The attitude norm error is calculated as

$$\|\delta\psi_k\| = \sqrt{\delta\theta_k^2 + \delta\phi_k^2 + \delta\varphi_k^2}.$$

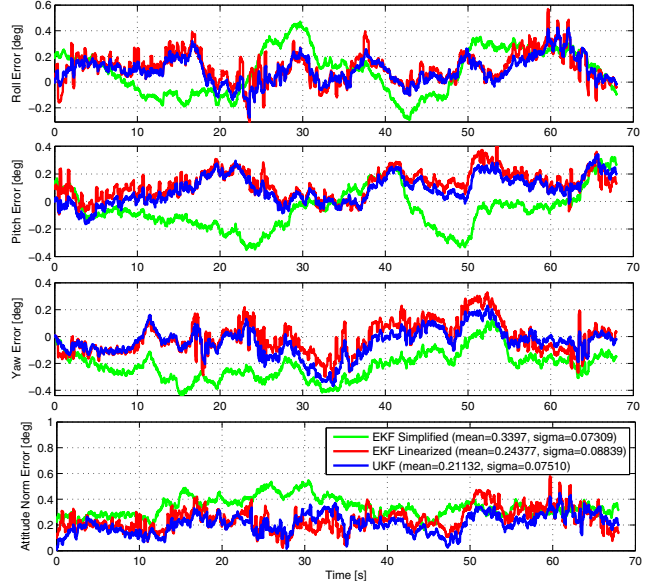


Figure 4. Attitude estimation errors (with calibrated Gyros)

As shown in the figure, the UKF and EKF with linearized system model show similar estimation results. This is because the main INS sensor errors (i.e., gyro bias) are corrected from the self alignment and calibration process. The green curves show the attitude estimation errors from the EKF with the simplified model. They do not follow the curves from the former two methods, and the estimation accuracy is also slightly worse. That is because the trajectory used in this simulation contains high dynamics. As shown in Figure 3, the angular rate

measurement from x axis reaches 50 deg/s from time to time. This leads the small angle assumption to be poor. However, the attitude errors are still bounded.

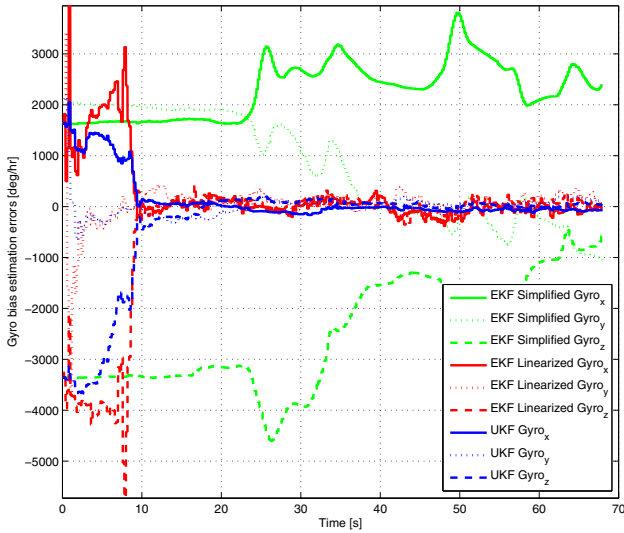


Figure 5. Gyro bias estimation errors (with un-calibrated Gyros).

Figure 5 shows the case that without INS self alignment and calibration processes, using the UKF and EKF with linearized system model, the gyro bias errors are correctly estimated. The curves in the figure represent the difference between the true simulated gyro biases and the estimated gyro biases. If the gyro biases are correctly estimated, these residuals will approach zero.

The advantage of using UKF can be observed, especially in the converging process. The EKF with simplified model does not work at all. It is because the gyro bias errors simulated in this test are large, (i.e., 3600 deg/hr as one sigma value), these gyro bias errors are contained in the gyro angular rate measurements, which makes the small angle assumption invalid.

5 Field Test

A field test is conducted based on the train from the city of Betzdorf to Siegen in Germany. The trajectory lasts 800 s. Only the UKF and EKF with linearized system model are considered in this test. One LandmarkTM20 MEMS-based IMU (100Hz) and one Ublox Antaris 4 (1Hz) GPS receiver are used. The trajectory contains 4 tunnels (GPS outages). The navigation solution from processing the raw data of a Ublox Antaris 4 GPS receiver using a least squares estimation method is presented in Figure 7. The number of tracked satellites is shown in the lower subplot of Figure 7.

The horizontal velocity estimates of INS/GPS integration system using the UKF are given in Figure 8. The INS bridges the GPS outage successfully. The IMU raw data are given in Figure 9.

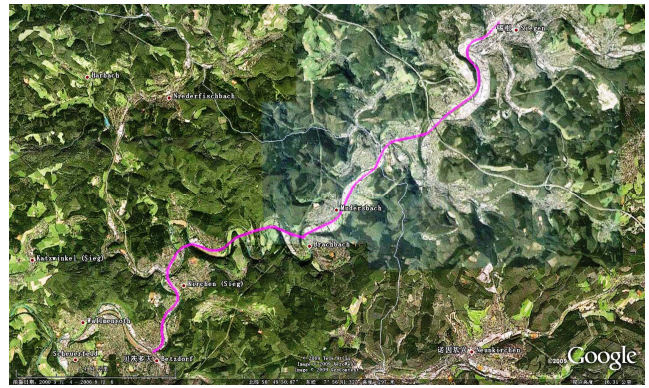


Figure 6. Field experiment trajectory.

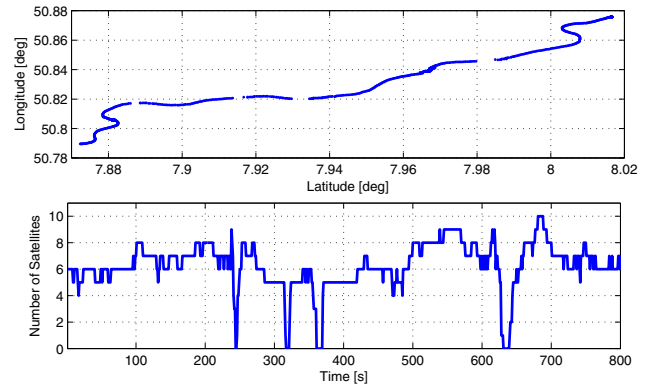


Figure 7. GPS signal conditions.

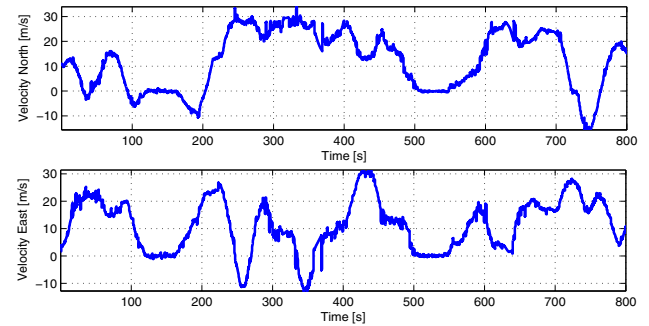


Figure 8. Velocity estimates in horizontal plane.

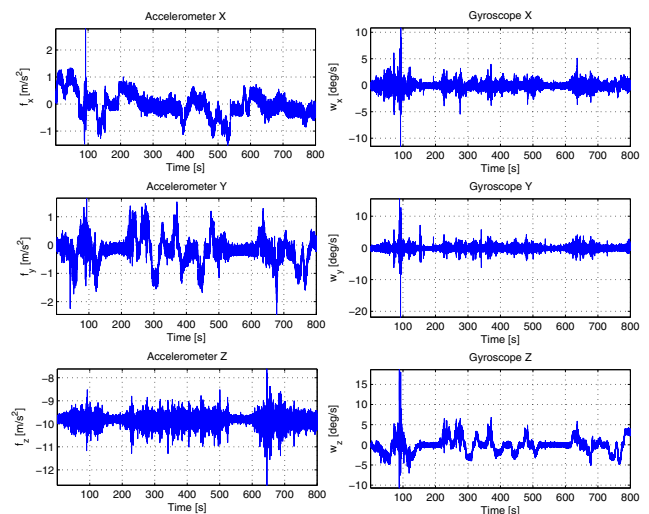


Figure 9. LandmarkTM20 raw data.

The estimated gyro bias errors are depicted in Figure 10. Both the EKF and UKF are tuned to trust more on the GPS measurements by giving relatively larger diagonal parameters in the process error covariance matrix \mathbf{Q} in the KF. No specific self alignment and calibration processes have been conducted before the experiment starts, and the gyro bias errors are unknown. The GPS pseudorange and Doppler measurements derived from the Ublox Antaris 4 GPS receiver are poor. Thus, we use 100 m for pseudorange and 0.1 m/s for Doppler as diagonal parameters in the measurement error covariance matrix \mathbf{R} .

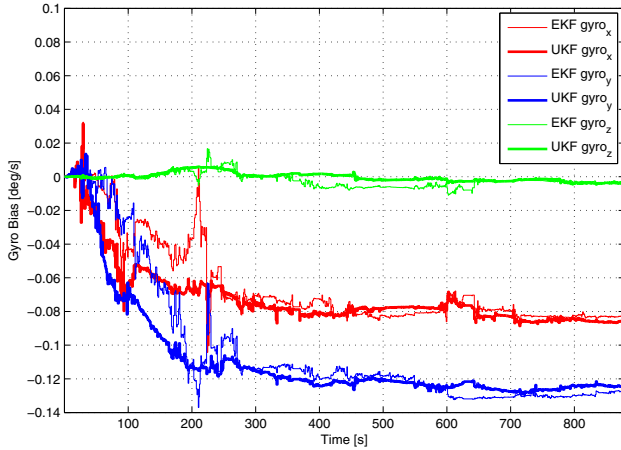


Figure 10. Estimated Gyro biases.

As shown in the figure 10, the UKF presents improved estimation performance as compared with the EKF, especially in the system converging process. If larger error covariance parameters are used in \mathbf{R} with smaller parameters used in \mathbf{Q} , both curves will be smoother, nevertheless, it will take more time for the filters to converge. Under the current setting, after 200 s, the estimated gyro bias errors from both methods have converged to approximately the same values.

The INS/GPS (UKF) estimated and gyro accumulated Euler angles are plotted in Figure 11. For land vehicle applications, the yaw angle can normally be derived from the north and east velocity estimates, i.e., $\varphi = \text{atan2}(v_E/v_N)$. The angles calculated by atan2 are limited to the interval between -180 to +180 degrees. However, they are transformed to 0 to 360 degrees to comply with the readings from LandmarkTM20 IMU. Due to the calculation of tangent (i.e., $\tan(\varphi) = \frac{\sin(\varphi)}{\cos(\varphi)} = \frac{v_E}{v_N}$),

when both the north and east velocities are approaching zero from either positive or negative side due to the measurement noises, (i.e., two stops are made by the train from 120 s to 160 s and 500 s to 550 s, where actually both the north and east velocities are nearly zero, as shown in Figure 8), the yaw estimates in these periods are completely wrong, as shown in Figure 11.

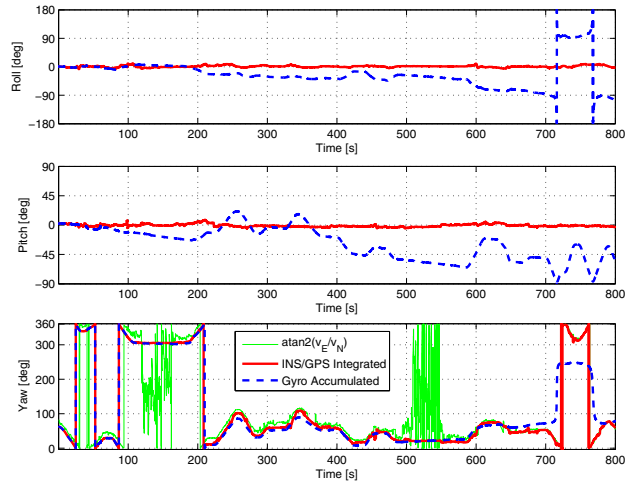


Figure 11. Estimated and Gyro accumulated Euler angles.

For the standalone INS, the gyro sensor errors (i.e. sensor bias and noise errors) are integrated to yield the Euler angle errors, as shown in Figure 11, which are drifting over time. When the pitch angle approaches ± 90 degrees, a singularity problem will appear. As shown in Equation (2), the definition of roll angle is proportional to $\text{Tangent}(\text{Pitch})$, and yaw angle is proportional to $1/\text{Cosine}(\text{Pitch})$. This means that the roll and yaw angles will be undefined at ± 90 degrees pitch angle. And large errors will occur when the pitch angle is approaching ± 90 degrees. For the INS/GPS integrated system, the Euler angles do not drift at all. That is because the sensor bias errors are correctly estimated, as shown in Figure 10. This also proves that the gyro bias errors are the dominant source of errors in the attitude determination for a low-cost INS/GPS integrated system.

The Euler angles estimated from the EKF and UKF algorithms are plotted in Figure 12. The readings from the magnetometers mounted inside of the LandmarkTM20 IMU are used to initialize the integrations (i.e., the initial Euler angles in Figure 12 are not zeros). Nevertheless, the system performances from the magnetometers depend largely on the environment. And there is no proof to say that its attitude solution can be better than the attitude estimates from the INS/GPS tightly-coupled integration. Therefore, we cannot use it as reference. We show the attitude estimation solutions from the EKF and UKF algorithms in Figure 12 directly.

With approximately correctly initialized attitude information, the EKF and UKF present similar system performances on attitude determination (i.e., no convergence process). However, we believe that the UKF presents better estimation results than the EKF for two reasons. Firstly, the gyro bias errors are faster and more smoothly estimated by the UKF algorithm, as shown in Figure 10. And secondly, large multipath effects will yield large innovation sequences in the KF. The UKF can achieve at least the 2nd order estimation accuracy from the Taylor series expansion, while the EKF is only at the first order accuracy, which causes the system performances

from the EKF more easily to be degraded by the external disturbances.

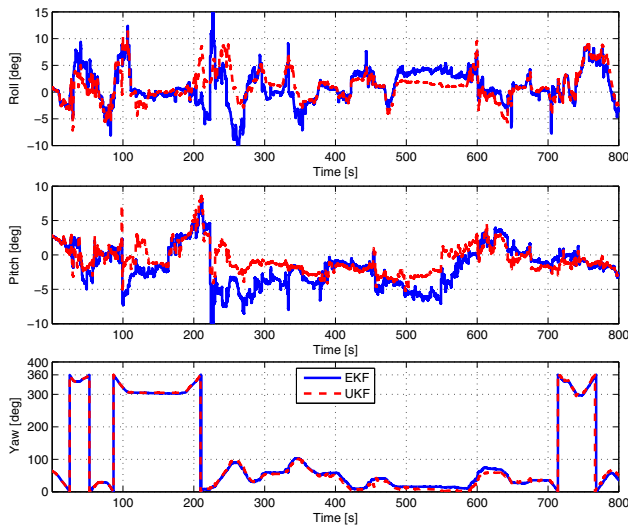


Figure 12. Euler angles estimated using EKF and UKF.

One disadvantage of the UKF algorithm is its higher processing load. The computer utilized for fusing the GPS and INS data in this paper is equipped with an Intel Core2Extreme X6800 CPU (2x2.93GHz) with 2GB DDR2 RAM. MATLAB R2009b is used. The computational time of the EKF for processing the whole set of collected GPS (1Hz) and IMU (100Hz) data is 85 s. For the UKF, it takes 233 s. The computational burden from the UKF is mainly coming from the time update part of the algorithm, which is at the IMU data update rate (100Hz). That is, the filter needs to pass $2 \cdot n$ (i.e., n is the dimension of the state vector, and in our case it is 17) sigma points through the nonlinear system model at 100 Hz update rate. For reducing this processing load, we can use the EKF linearized system model at the time update of KF, and apply the UKF algorithm in the measurement update phase of the KF, which is at the GPS measurement update rate (1Hz). The system performance from such a combination has not yet been investigated, which leads to the future work.

Conclusion

In an INS/GPS integrated navigation system, the system models are highly nonlinear. Three Kalman filtering methods are employed to investigate the influence of the nonlinearity on the system estimation performance. Simulations are conducted based on a high dynamic UAV trajectory, and a field experiment is made using the train. Numerical results show that using the UKF and EKF with linearized model, the gyro bias errors can be correctly estimated. For the EKF with simplified model, it works only when certain rules are met. The UKF presents improved estimation accuracy, especially in the convergence process and when large disturbances are presented on the GPS signals. However, its computational burden is significantly increased.

Acknowledgement

Part of the work reported herein has been funded by the German Science Foundation (DFG), grant number KN 876/1-2, which is gratefully acknowledged.

References

- [1] J.C. Zhou, S. Knedlik and O. Loffeld, *INS/GPS Tightly-coupled Integration using Adaptive Unscented Particle Filter*, The Journal of Navigation, Vol.63, No.3, July, 2010.
- [2] J.C. Zhou, S. Knedlik and O. Loffeld, *Tightly-coupled MEMS-INS/GPS Integration using Sequential Processing Method*, ION GNSS 2009, Savannah, Georgia, USA. September 16-19, 2009.
- [3] S. Knedlik, J.C. Zhou and O. Loffeld, *On position and attitude estimation for remote sensing with bistatic SAR*, Geoscience and remote sensing, In-Tech, Book chapter, pp. 75-90, Vukovar, 2009. <http://sciyo.com/books/show/title/geoscience-and-remote-sensing>
- [4] S.J. Julier and J.K. Uhlmann. *Unscented Filtering and Nonlinear Estimation*. IEEE Review, 92(3), March 2004.
- [5] J.A. Farrel, *Aided Navigation: GPS with High Rate Sensors*, McGraw-Hill, New York, 2008.
- [6] S. Sukkarieh, *Low Cost, High Integrity, Aided Inertial Navigation Systems for Autonomous Land Vehicles*, Ph.D Dissertation, University of Sydney.
- [7] D.H. Titterton and J.L. Weston (2004). *Strapdown Inertial Navigation Technology*, 2nd ed., Institution of Engineering and Technology.
- [8] P. Misra and P. Enge, *Global Positioning System, Signals, measurements, and Performance*, 2nd ed., Ganga Jamuna Press, Lincoln, 2006.
- [9] N. El-Sheimy and X. Niu, *The Promise of MEMS to the Navigation Community*, InsideGNSS, pp. 46-56, April 2007.
- [10] D. Simon, *Optimal State Estimation: Kalman, Hinfinity, and Nonlinear Approaches*, 1st ed., John Wiley and Sons., New Jersey, 2006.

Biography

Junchuan Zhou obtained the M.Sc.degree in Mechatronics from the University of Siegen, Germany, in 2006. He is currently pursuing his Ph.D. in Electrical Engineering within the International Postgraduate Programme (IPP) of Multi Sensorics at the Center for Sensorsystems (ZESS) in the University of Siegen. His current research interest is GPS/INS integration using nonlinear filtering methods.